

Anthropogenically-driven escalating impact of soil-based compound dry-hot extremes on vegetation productivity

Received: 13 February 2025

Accepted: 16 January 2026

Published online: 03 February 2026

 Check for updates

Yani Liang^{1,2}, Jun Wang¹✉, Zengchao Hao³, Huanjiong Wang¹,
Huijuan Cui¹ & Quansheng Ge^{1,2}✉

Compound dry-hot extremes exert stronger environmental impacts than individual dry or hot extremes. While evidence for increasing meteorological compound dry-hot extremes (defined using surface air temperature and vapor pressure deficit or precipitation) is growing, the impacts and evolving risks of soil-based compound dry-hot extremes remain poorly understood. Using homogenized soil temperature observations and observationally constrained soil moisture dataset for China, we show that the adverse effects of soil-based compound dry-hot extremes on vegetation productivity are more severe than their meteorological counterparts. From 1980 to 2017, the frequency and coverage area of soil-based compound dry-hot extremes in China increased by 3.0 days and $141.9 \times 10^4 \text{ km}^2$, respectively, with the most pronounced increases occurring in northern China. These increases are primarily attributed to anthropogenic soil warming. Under a fossil-fueled development scenario, the mean frequency of such extremes is projected to increase by 13.3 days by the end of the twenty-first century relative to the 1981–2010 baseline, potentially reducing China's terrestrial vegetation gross primary production by approximately $0.025 \text{ Pg C a}^{-1}$. Our findings highlight an anthropogenic escalation of soil-based compound dry-hot extremes and their growing threats to terrestrial carbon sinks and food security.

Concurrent dry and hot conditions can severely impact ecosystems, economies, and human societies by triggering a cascade of adverse effects, including reduced streamflow, water shortages, heat stress, crop failures, and wildfires^{1–6}. For instance, persistent record-breaking compound dry-hot extremes (CDHEs) struck southern China, Europe, and the western United States in 2022, suppressing vegetation growth, causing declines in crop yield, and inducing significant societal consequences^{7–9}. Most CDHEs occur in association with anomalous anticyclonic circulations and descending air motions¹⁰. These atmospheric circulation patterns reduce precipitation, enhance adiabatic heating, decrease cloud cover, and increase solar radiation,

collectively creating conditions conducive to the formation of CDHEs. In regions where soil moisture and temperature are strongly coupled, dry soils can further exacerbate hot extremes by weakening evaporative cooling^{11,12}.

While changes in soil hydrothermal conditions are key drivers of the development and intensification of CDHEs, most existing studies have focused solely on meteorological or atmospheric CDHEs, which are typically defined using surface 2-m air temperature paired with precipitation or air humidity-related metrics (e.g., vapor pressure deficit (VPD))^{5,13–16}, primarily because meteorological datasets are far more readily available than soil observational data. The construction,

¹Key Laboratory of Land Surface Pattern and Simulation, Institute of Geographic Sciences and Natural Resources Research, Chinese Academy of Sciences, Beijing, China. ²University of Chinese Academy of Sciences, Beijing, China. ³College of Water Sciences, Beijing Normal University, Beijing, China.

✉ e-mail: wangjun@igsnr.ac.cn; geqs@igsnr.ac.cn

operation, and maintenance of global soil monitoring networks are expensive and labor-intensive, leading to a scarcity of global-scale observations for soil temperature and moisture¹⁷. While some global databases (e.g., the FLUXNET2015 dataset¹⁸) provide high-quality observations of soil temperature and moisture at selected sites, their sparse and irregular spatiotemporal coverage limits their utility for high-resolution, large-scale, and long-term CDHE monitoring¹⁸. To address the limitations of in situ soil measurements, remote sensing has emerged as a key alternative approach. However, microwave-based soil parameter retrievals often suffer from spatial incompleteness, with striping gaps arising from constraints related to satellite scanning patterns, orbital paths, and retrieval algorithms¹⁹, which compromise their reliability and broader applicability. The scarcity of soil data, coupled with the long-standing prevalence of a canonical meteorological perspective, has hindered research into soil-based CDHEs, which are characterized by anomalous soil temperature and moisture conditions. While some CDHE studies have incorporated soil moisture or terrestrial water storage to characterize dry extremes^{20,21}, hot extremes in these works were still defined using surface 2-m air temperature. A recent study highlighted the uniqueness of soil thermal dynamics, finding that in Central Europe, soil hot extremes are intensifying 0.7 °C per decade faster than air hot extremes and increasing twice as rapidly in frequency²². Nevertheless, the evolving risks of soil-based CDHEs and their underlying driving mechanisms remain underexplored.

In terms of ecological impacts, soil moisture and temperature regulate numerous biogeochemical processes in vegetation and soil systems. For instance, it has been proposed that in most vegetated areas, soil moisture plays a relatively more dominant role in dryness stress on vegetation productivity compared to VPD²³. Furthermore, over the past four decades, vegetation leaf area index is increasingly sensitive to soil moisture in many water-constrained and drying regions²⁴. Beyond moisture effects, plant physiological processes are more closely linked to below-canopy soil temperature than to surface 2-m air temperature²⁵. Notably, soil temperature acts as a dominant driver of spring phenology variations in approximately half of China's forested areas²⁶. Additionally, soil moisture and temperature jointly modulate vegetation growth and productivity by regulating soil microbial and enzymatic activities, as well as the availability of water and nutrients to both plants and microbes^{27,28}. Despite accumulating evidence highlighting the higher sensitivity of terrestrial vegetation to soil moisture and temperature (relative to atmospheric metrics), the impacts of soil-based CDHEs on vegetation productivity under a changing climate remain inadequately evaluated.

Here, we assess the impacts of soil-based CDHEs on terrestrial vegetation productivity and compare these impacts with those of meteorological CDHEs using newly homogenized soil temperature observations for China, an observationally constrained soil moisture dataset, and observation-based datasets of gross primary production (GPP), solar-induced chlorophyll fluorescence (SIF), and net primary production (NPP). We also develop an analytical framework to conduct quantitative attribution analyses of the observed changes in the frequency and spatial coverage of soil-based CDHEs, with the aim of isolating the individual contributions of anthropogenically-driven changes in soil temperature and moisture. Furthermore, we investigate future changes in soil-based CDHE risks across different land cover types in China using a single model initial-condition large ensemble. On this basis, we estimate the associated potential impacts of these changes on China's terrestrial vegetation productivity.

Results

More severe adverse impacts of soil-based CDHEs on vegetation productivity

We first calculate composite GPP and SIF anomalies during soil-based CDHEs in the warm season (from May to September) (Methods). Our

results show that GPP and SIF anomalies are negative across most vegetated areas in China during soil-based CDHEs (Fig. 1a, b). The spatial patterns of GPP and SIF responses to these events are highly analogous, with a statistically significant spatial correlation coefficient of 0.88 ($p < 0.01$). Pronounced negative anomalies are observed across large swaths of northern and southwestern China. In contrast, northern Northeast China exhibits slightly positive GPP and SIF anomalies during soil-based CDHEs (Fig. 1a, b). This may be because higher temperatures in this cold and humid region can enhance vegetation photosynthetic efficiency²⁹. Given the strong correlation between GPP and SIF anomalies, we further compute composite NPP anomalies during warm-season soil-based CDHEs to better understand the impact of soil-based CDHEs on vegetation productivity. The pattern of NPP responses to soil-based CDHEs is consistent with those of GPP and SIF (Supplementary Fig. 1), with nearly all vegetated areas exhibiting negative NPP anomalies during such extremes. Collectively, these results indicate that soil-based CDHEs exert adverse impacts on vegetation productivity across most of China's vegetated areas.

To compare vegetation productivity anomalies during soil-based CDHEs with those under other soil hydrothermal conditions, we categorize daily surface soil temperature and moisture into 10×10 percentile bin combinations for each grid cell and then compute their corresponding mean occurrence frequencies across all grid cells with valid values (Methods). The mean occurrence frequency exhibits a bimodal joint distribution of soil temperature and moisture, with peaks under dry-hot and wet-cold conditions (Fig. 1c). Among all combinations, the likelihood of soil-based CDHE occurrence is the highest, with a likelihood multiplication factor (LMF—a metric used to quantify the effect of variable dependence on the likelihood of a compound event³⁰) of 2.5. This result underscores the effect of soil moisture-temperature coupling on the formation of soil-based CDHEs.

We then compute composite mean GPP and SIF anomalies for each percentile bin combination of soil temperature and moisture (Methods). Under relatively hot and wet soil conditions, GPP and SIF anomalies are predominantly positive. As soil dryness increases, however, these anomalies shift from positive to negative, becoming markedly negative under dry-hot soil conditions (Fig. 1d, e). Notably, the low-right bin (representing extreme soil dryness and heat) exhibits the most negative GPP and SIF anomalies of $-0.186 \text{ g C m}^{-2} \text{ d}^{-1}$ and $-0.013 \text{ mW m}^{-2} \text{ nm}^{-1} \text{ sr}^{-1}$, respectively. This finding indicates that the adverse effects of soil hydrothermal stress on vegetation productivity are most pronounced during soil-based CDHEs.

Furthermore, we compare vegetation productivity anomalies during meteorological CDHEs, which are identified based on surface 2-m air temperature and VPD (Methods). Only minor negative GPP and SIF anomalies associated with meteorological CDHEs are observed in northeastern China (Supplementary Fig. 2a, b), indicating that vegetation productivity responses to meteorological CDHEs are much weaker than those to soil-based CDHEs. Surface 2-m air temperature and VPD are strongly interrelated, as reflected by a LMF of 8.2 for meteorological CDHEs (Supplementary Fig. 2c), which is significantly higher than that for soil-based CDHEs (Fig. 1c). Notably, the most negative GPP and SIF anomalies are not associated with meteorological CDHEs (Supplementary Fig. 2d, e). Thus, compared with soil-based CDHEs, the adverse impacts of meteorological CDHEs on vegetation productivity are generally weaker (Fig. 1d, e vs. Supplementary Fig. 2d, e).

To disentangle the relative roles of soil temperature and moisture in driving the divergent vegetation productivity responses to soil-based and meteorological CDHEs, we calculate composite GPP and SIF anomalies during soil-air blended CDHEs, which are defined using soil temperature and VPD. The spatial patterns of vegetation productivity anomalies during soil-air blended CDHEs are similar to those during soil-based CDHEs (Fig. 1a, b and Supplementary Fig. 3a, b). However,

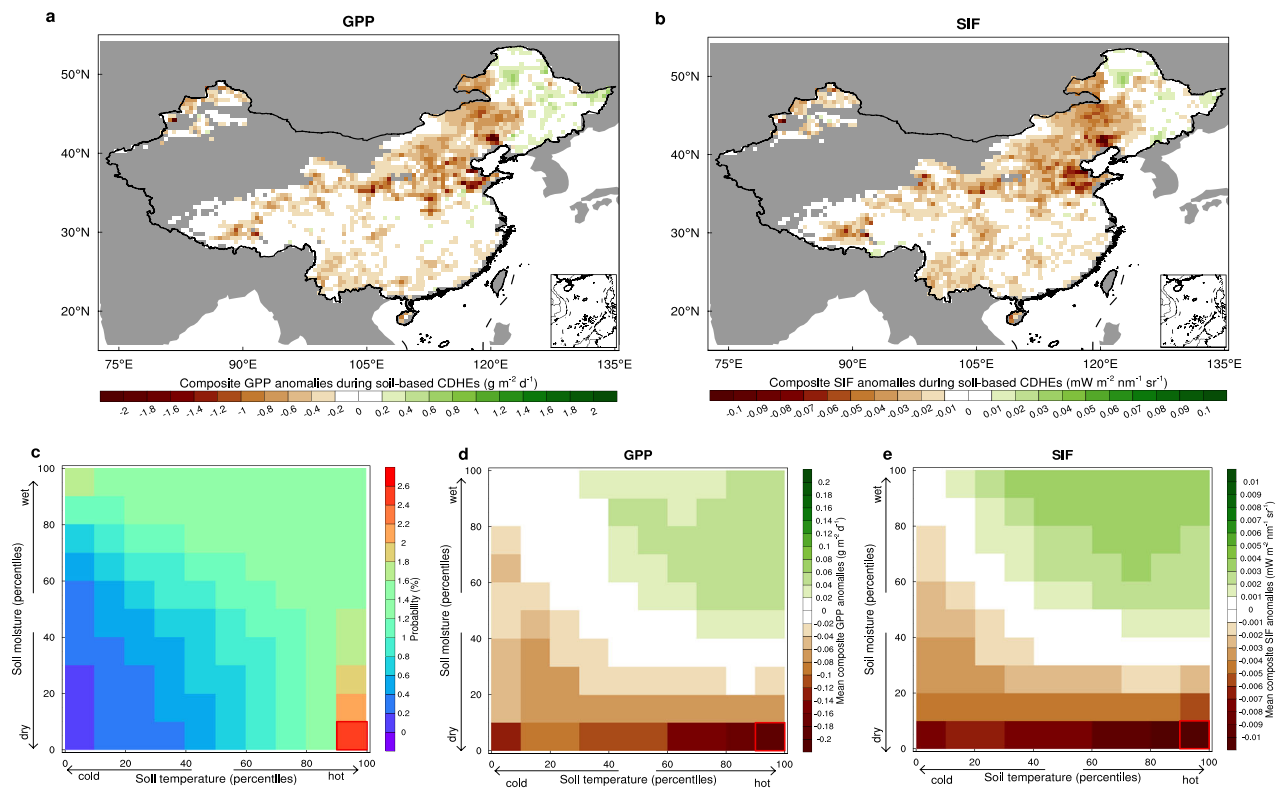


Fig. 1 | Responses of gross primary production and solar-induced fluorescence to soil-based compound dry-hot extremes (CDHEs). Composite anomalies of gross primary production (**a**; GPP expressed as carbon hereafter) and solar-induced fluorescence (**b**; SIF) during soil-based CDHEs in China. **c** Mean probability of occurrence of each percentile bin combination of surface soil temperature (*x*-axis) and soil moisture (*y*-axis) across all valid grid cells in China. Mean composite

anomalies of GPP (**d**) and SIF (**e**) for each percentile bin combination of soil temperature (*x*-axis) and soil moisture (*y*-axis) across all valid grid cells in China. The red box denotes the grid-mean composite anomaly during soil-based CDHEs (soil temperature higher than the 90th percentile and soil moisture lower than the 10th percentile).

compared with soil-based CDHEs, the magnitudes of negative GPP and SIF anomalies associated with soil-air blended CDHEs are much smaller. Since the only difference between the definitions of soil-based CDHEs and soil-air blended CDHEs lies in their dryness metrics (soil moisture vs. VPD), this finding indicates that low soil water supply may impose higher dryness stress on vegetation productivity than high atmospheric moisture demand. Furthermore, compared with meteorological CDHEs, soil-air blended CDHEs correspond to slightly larger magnitudes of negative GPP and SIF anomalies (Supplementary Figs. 2d, e and 3d, e). This implies that soil hot extremes may exert slightly greater heat stress on vegetation productivity than atmospheric hot extremes.

Beyond VPD, we also define CDHEs based on the Standardized Precipitation Evapotranspiration Index (SPEI)³¹, using a global multi-timescale daily SPEI dataset (Methods). We first select two SPEI timescales (5 days and 30 days) to capture short-term water deficits induced by meteorological droughts. For both 5-day and 30-day SPEI-based CDHEs, the composite GPP and SIF anomalies are smaller than those associated with soil-based CDHEs (Fig. 1a, b and Supplementary Fig. 4). In contrast, when CDHEs are defined using SPEI with extended timescales of 90 days and 180 days (typically representing soil or agricultural droughts), the composite GPP and SIF anomalies are comparable to those linked to soil-based CDHEs (Fig. 1a, b and Supplementary Fig. 5). This aligns with previous findings that the 6-month SPEI (consistent with the 180-day timescale used here) exhibits the strongest correlation with soil moisture^{32,33}. Taken together, our results suggest that soil-based CDHEs generally exert more severe adverse impacts on vegetation productivity than meteorological CDHEs, primarily through soil dryness.

Rapid increase in soil-based CDHEs

From 1980 to 2017, the annual mean frequency and spatial coverage area of soil-based CDHEs in China increased by 3.0 (1.5–4.5) days and $141.9 (19.2–264.7) \times 10^4 \text{ km}^2$, respectively. More substantial increases are observed in northern China, the Central Plains, and parts of southwestern China (e.g., eastern Tibetan Plateau) (Fig. 2). The rapid increase in soil-based CDHEs in northern China and eastern Tibetan Plateau is closely linked to strong soil warming in these regions (Supplementary Fig. 6a). Beyond soil warming, the increased CDHE frequency in northern Northeast China and the Central Plains is also associated with a long-term decline in soil moisture (Supplementary Fig. 6b). In contrast, the decreased frequency of soil-based CDHEs in parts of southern China appears to stem from a moderate soil wetting trend, coupled with little long-term change in soil temperature (Supplementary Fig. 6).

The geographic patterns of trends in soil temperature and surface 2-m air temperature are highly similar, with a statistically significant spatial correlation coefficient of 0.59 ($p < 0.01$; Supplementary Figs. 6a and 7a). The regionally heterogeneous trends in soil moisture can be partially explained by spatial variations in warm-season precipitation trends (Supplementary Figs. 6b and 7b), as indicated by a spatial correlation coefficient of 0.31 ($p < 0.01$) between the two variables.

Although changes in soil temperature and moisture are well aligned with changes in the frequency of soil-based CDHEs, the root causes of regional inhomogeneity in soil-based CDHE frequency trends lie in the changes of large-scale atmospheric circulations and soil moisture-temperature coupling. From 1980 to 2017, the warm-season mean eddy geopotential increased

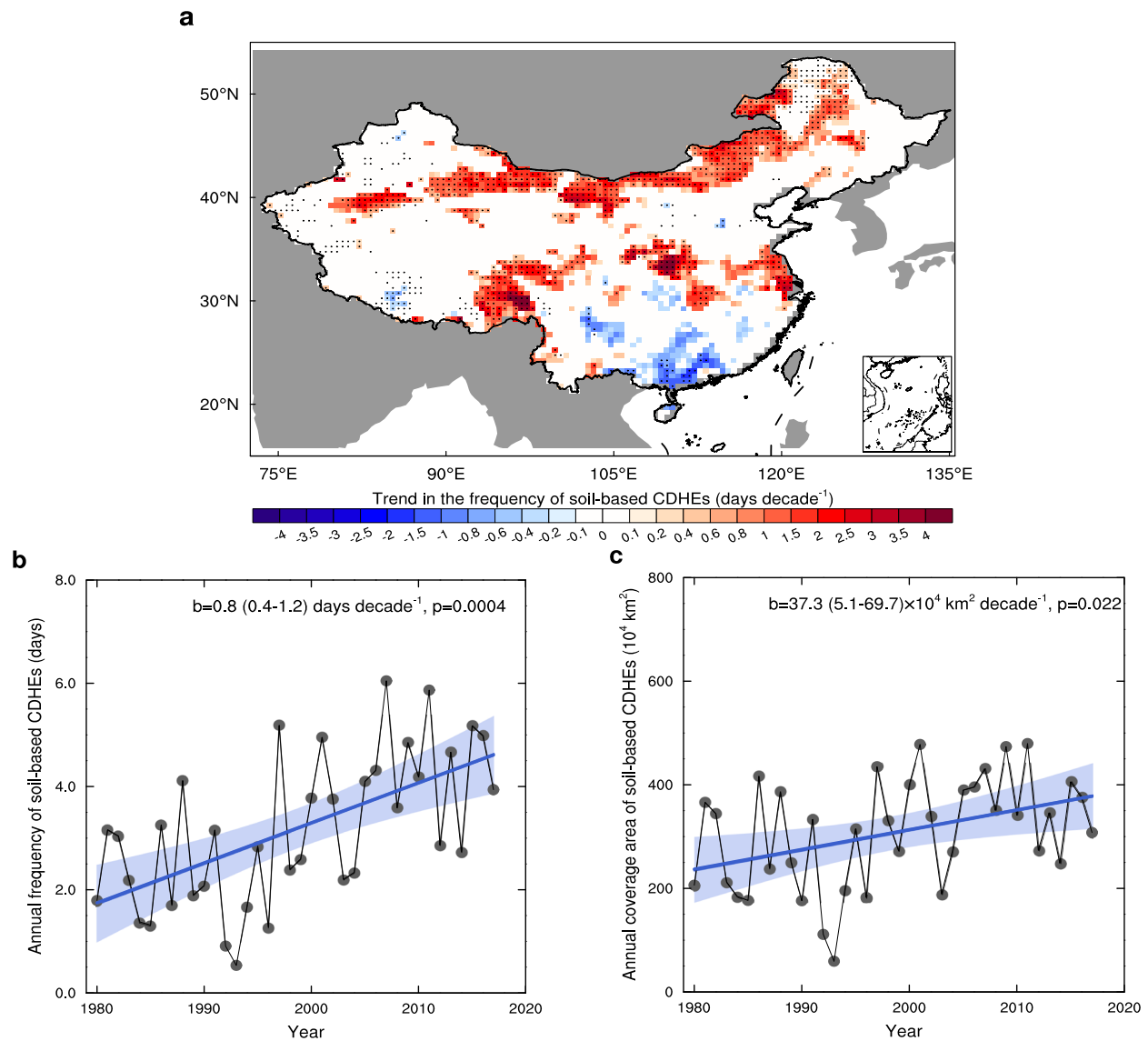


Fig. 2 | Rapid increase in soil-based compound dry-hot extremes (CDHEs).

a Spatial pattern of linear trends in the annual frequency of soil-based CDHEs in China over 1980–2017 (dots denote statistically significant trends based on the two-sided Mann–Kendall trend test, $p < 0.01$). **b** Time series of the regional area-weighted mean frequency of soil-based CDHEs over 1980–2017. **c** Time series of the spatial coverage area of soil-based CDHEs in China over 1980–2017. A grid cell is

defined as part of the affected area if it experiences at least three soil-based CDHE days during a given warm season. The blue line represents the linear regression slope, with blue shading indicating its 95% confidence interval. The linear regression slope (b), its 95% confidence interval (values in parenthesis), and p -value (p) are shown.

significantly over northern China and Mongolia, leading to a substantial growth of anticyclonic circulation conditions (Fig. 3a). Anomalous anticyclonic circulations promote increased adiabatic heating and incoming solar radiation, which readily warm both surface soils and the near-surface atmosphere. Furthermore, northern and northeastern China exhibit an increasing trend in soil moisture-temperature coupling strength (Methods; Fig. 3b). In these wet-to-dry transitional regions, hotter soil and air temperatures can rapidly deplete surface soil water, increasing soil evaporation and atmospheric water demand^{34,35}. In turn, drier soil conditions can further warm surface soils by enhancing land sensible heat flux and reducing soil heat capacity^{36,37}. Notably, in hotspot regions where soil-based CDHE frequency is increasing rapidly (Fig. 2a), the amplified soil moisture-temperature coupling coincides with a more pronounced increase in anticyclonic activity (Fig. 3a, b). For northern China specifically, the annual frequency of soil-based

CDHEs is strongly correlated with eddy geopotential and soil moisture-temperature coupling strength, with statistically significant temporal correlation coefficients of 0.52 and 0.64 ($p < 0.01$), respectively (Fig. 3c). In contrast, southern China has experienced shifts toward cyclonic circulation at 500 hPa, alongside little change in soil moisture-temperature coupling strength (Fig. 3a, b). These circulation changes favor ascending air motions and increased precipitation, which in turn drive soil wetting trends. Increased soil moisture can weaken soil warming by boosting evaporative cooling. These combined changes are the direct drivers of the observed decline in soil-based CDHE frequency in southern China (Fig. 2a). Collectively, these correlation analysis results indicate that changes in large-scale atmospheric circulations and soil moisture-temperature coupling may jointly contribute to the observed regional heterogeneity in soil-based CDHE frequency trends in China (Fig. 3d).

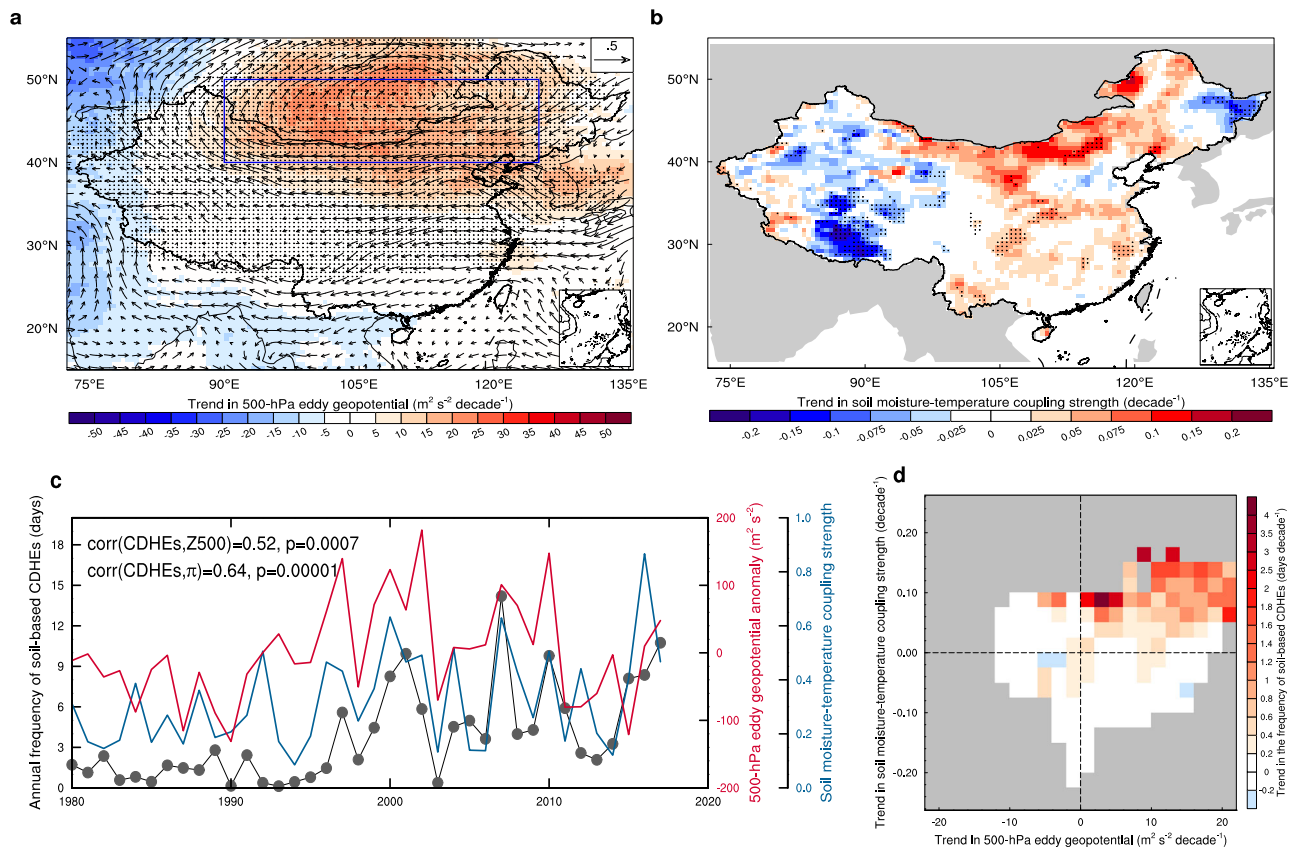


Fig. 3 | Dependence of frequency trend pattern on physical drivers. **a** Spatial patterns of linear trends in warm-season (from May to September) mean 500-hPa eddy geopotential (Z500; shading) and winds (vector) over 1980–2017. The blue rectangle encompasses the northern part of China and its surrounding regions (90°E–125°E; 40°N–50°N), where the increasing frequency trend of soil-based compound dry-hot extremes (CDHEs) is the most pronounced. **b** Spatial distribution of linear trends in warm-season soil moisture-temperature coupling strength over 1980–2017. Dots in **(a, b)** denote statistically significant trends based on the two-sided Mann–Kendall trend test ($p < 0.01$). **c** Time series of warm-season soil-based CDHE frequency (gray dots), mean Z500 anomaly (red line), and mean soil

moisture-temperature coupling strength (π ; blue line) averaged over the northern part of China from 1980 to 2017. Pearson's correlation coefficients (corr) between soil-based CDHE frequency and Z500 anomaly/ π , along with their p -values (p), are shown. **d** Joint impacts of changes in atmospheric dynamics and soil moisture-temperature coupling on soil-based CDHE frequency trend patterns. Trends in 500-hPa eddy geopotential (x -axis) and soil moisture-temperature coupling strengths (y -axis) are binned into the intervals of $2 \text{ m}^2 \text{ s}^{-2} \text{ decade}^{-1}$ and $0.025 \text{ decade}^{-1}$, respectively. The color of each grid indicates the composite frequency trend averaged over the grid cells where Z500 and π trends fall into the corresponding bins.

Anthropogenic soil warming drives the surge in soil-based CDHEs

Very few climate models participating in the Detection and Attribution Model Intercomparison Project³⁸ contributed to the sixth phase of the Coupled Model Intercomparison Project (CMIP6)³⁹ provide both daily soil temperature and moisture data. As a result, the observed changes in soil-based CDHEs cannot be directly attributed to anthropogenic or natural forcings. Furthermore, estimates of soil-based CDHE frequency and coverage area derived from a limited number of model realizations are highly uncertain at the regional scale, primarily due to strong internal climate variability and substantial sampling uncertainty^{14,40}. To address these challenges, we develop an analytical framework to attribute anthropogenic influences on the observed increase in soil-based CDHEs by focusing on disentangling the individual contributions of anthropogenically-driven changes in soil temperature and moisture (Methods).

We calculate multi-model ensemble (MME) mean anomalies of soil temperature and moisture simulated by the experiments driven by all historical external forcings (ALL) and natural forcing only (NAT) (Supplementary Fig. 8a). Our results show that ALL-forced simulations can well reproduce the observed warm-season soil temperature changes in China, although the observed soil warming trend is slightly stronger than the ALL-forced MME mean trend (0.49 vs. 0.34 °C per

decade). Since most internal climate variability is averaged out in the MME mean, the residual difference in soil temperature trends between observations and ALL-forced simulations can be partly attributed to internal climate variability-related atmospheric circulation changes, such as the increasing anticyclonic conditions over northern China (Fig. 3a). In contrast, NAT-forced simulations fail to reproduce the observed soil warming trend (Supplementary Fig. 8a).

Notably, the magnitudes and spatial patterns of soil temperature trend differences between ALL- and NAT-forced simulations are highly consistent with the observed soil warming trends (Supplementary Figs. 6a and 8c), as evidenced by a significant spatial correlation coefficient of 0.73 ($p < 0.01$). This implies that anthropogenic forcings—dominated by anthropogenic greenhouse gases and aerosols—play a dominant role in driving the observed soil warming in China. However, ALL-forced simulations fail to reproduce the observed soil moisture changes (Supplementary Fig. 8b). The ALL-forced MME mean soil moisture trend is nearly zero, substantially weaker than the observed trend (Supplementary Fig. 8b). This discrepancy arises because anthropogenic forcings induce positive soil moisture trends in central-eastern and northern China but negative trends across large swaths of southwestern China (Supplementary Fig. 8d). These opposing trends offset each other, resulting in a near-zero regional mean soil moisture trend. In other words, anthropogenic forcings contribute little to the

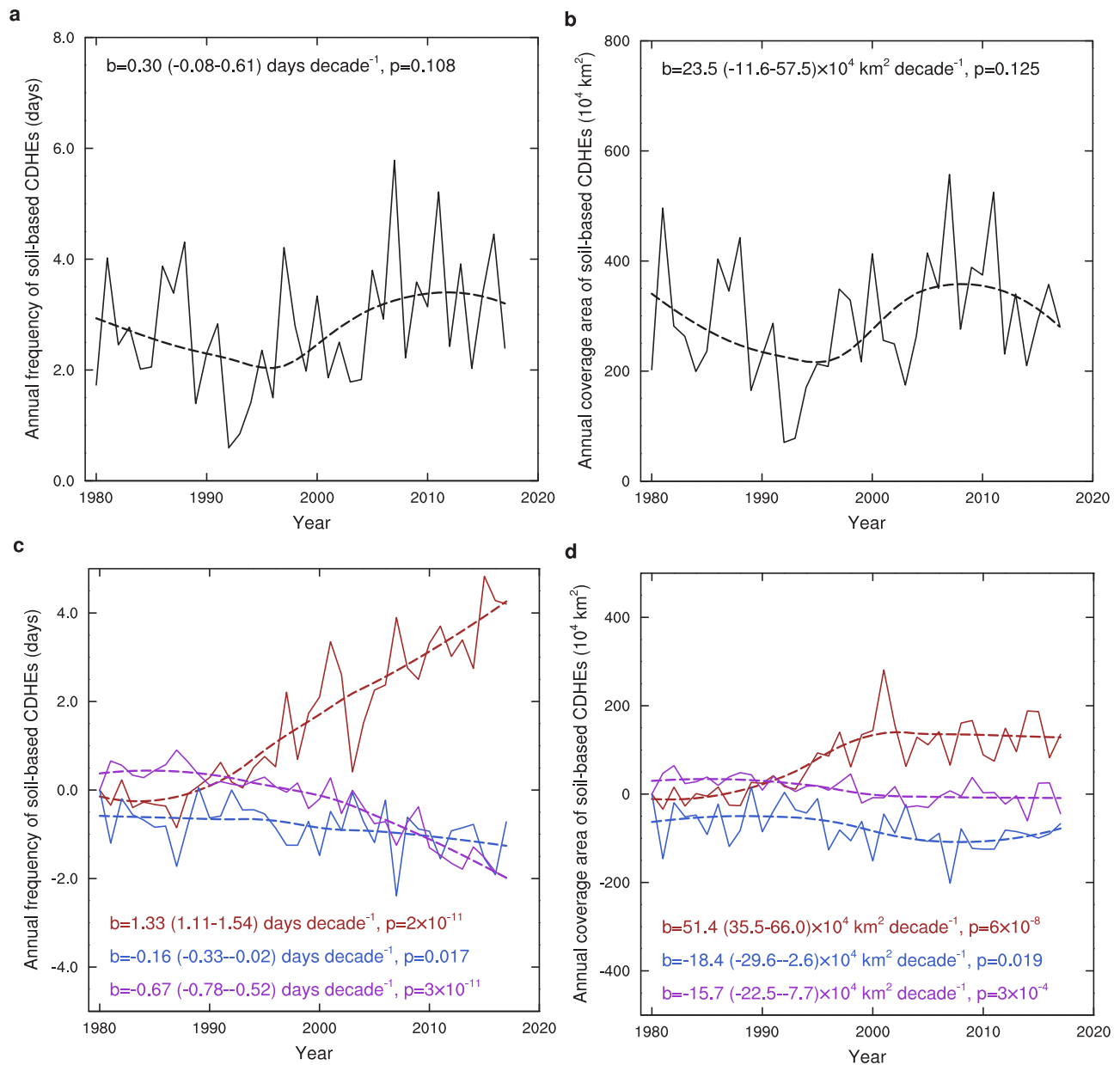


Fig. 4 | Critical role of anthropogenic soil warming in the surge of soil-based compound dry-hot extremes (CDHEs). **a** Observed regional mean annual frequency of soil-based CDHEs over 1980–2017 in China with anthropogenically-induced changes in soil temperature and moisture removed. **b** Same as **(a)**, but for the annual coverage area of soil-based CDHEs. A grid cell is defined as part of the affected area if it experiences at least three soil-based CDHE days during a given warm season. **c** Regional mean annual frequency of soil-based CDHEs over 1980–2017 in China driven by anthropogenically-induced changes in soil temperature (red line), anthropogenically-induced changes in soil moisture (blue line), and nonlinear interactions between them (purple line), respectively. **d** Same as **(c)**, but for the annual coverage area of soil-based CDHEs. The dashed line represents

smoothed variations derived from LOESS local regression with a default span of 0.75. The linear regression slope (**b**), its 95% confidence interval (values in parenthesis), and *p*-value (*p*) are shown. The statistical trend analyses are conducted using the two-sided Mann–Kendall trend test. Since the effects of anthropogenic soil temperature and moisture changes on soil-based CDHE changes are represented by the estimated differences between different datasets (adjusted vs. unadjusted datasets), some time series of CDHE frequency and coverage area contain negative values. Nevertheless, our analysis focuses on long-term trends. Note that linear trends are computed using the non-parametric Theil–Sen trend estimation method, and thus the sums of these four components differ slightly from the trends shown in Fig. 2b, c.

observed regional mean soil moisture trend in China but exert a certain influence on local soil moisture trends.

We remove anthropogenically-driven spatiotemporal changes in soil temperature and moisture from the observational data and then recalculate the frequency and spatial coverage area of soil-based CDHEs in China (Methods). With anthropogenically-forced signals eliminated, the recalculated changes in soil-based CDHEs are dominated by natural climate variability. Natural variability-induced

soil-based CDHE frequency and coverage area exhibit a declining trend from the 1980s to the mid-1990s, followed by an increase from the mid-1990s to the late 2000s, and another decline after 2010 (Fig. 4a, b). These variations are likely linked to the Atlantic Multidecadal Oscillation⁴¹. Over the past four decades, natural climate variability may have increased the frequency and coverage area of soil-based CDHEs in China by 1.1 days and $89.3 \times 10^4 \text{ km}^2$, respectively.

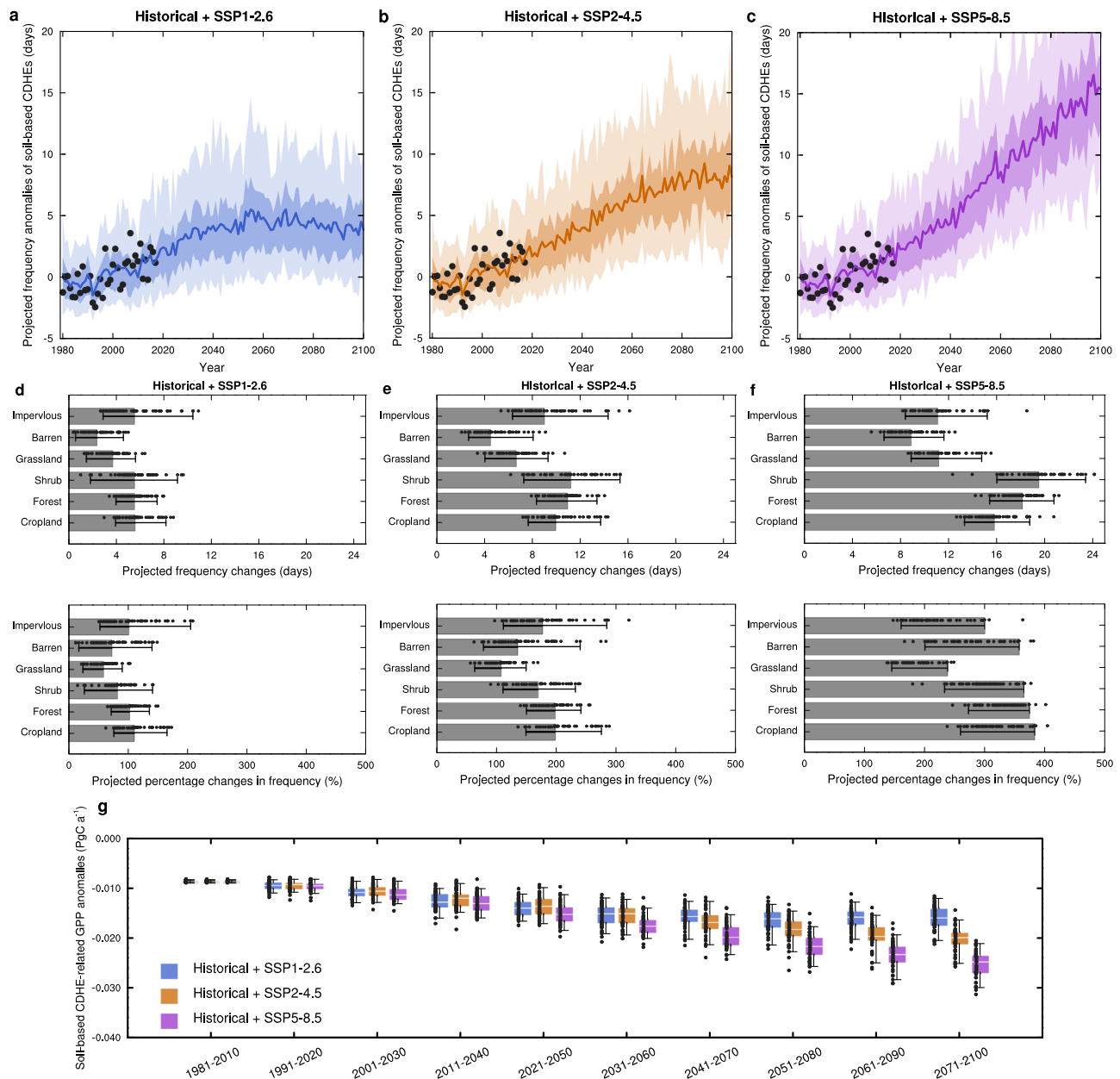


Fig. 5 | Future changes in the frequency of soil-based compound dry-hot extremes (CDHEs) across six major land cover types and their implications for China's terrestrial vegetation productivity. Area-weighted mean time series of observed, simulated, and projected frequency anomalies (relative to the 1981–2010 historical baseline) of soil-based CDHEs in China under SSP1-2.6 (a), SSP2-4.5 (b), and SSP5-8.5 (c). Black dots represent observational data points. Solid line denotes the ensemble median of simulated and projected frequency anomalies, with dark and light shadings indicating the interquartile range (IQR) and the 5–95% range of ensemble members, respectively, reflecting the scope of internal climate variability. Projected area-weighted mean frequency changes (relative to 1981–2010) of soil-based CDHEs by the end of the twenty-first century (2071–2100) under SSP1-2.6 (d), SSP2-4.5 (e), and SSP5-8.5 (f) for six major land cover types in China. The upper

panel shows absolute frequency changes, and the lower panel displays percentage changes in frequency (relative to 1981–2010). Gray bar represents the ensemble median, with the black whiskers indicating the 5–95% range of ensemble members. The corresponding data points are overlaid. **g** Estimated changes in total vegetation gross primary production anomalies associated with soil-based CDHEs in China under SSP1-2.6 (blue), SSP2-4.5 (orange), and SSP5-8.5 (purple). These empirical projections assume that the magnitudes and pattern of vegetation gross primary production responses to soil-based CDHEs (as shown in Fig. 1a) remain unchanged in the future. White line denotes the ensemble median, with colored box and black whiskers indicating the IQR and the 5–95% range of ensemble members. The corresponding data points are overlaid. The number of ensemble members is $n = 50$.

We then recalculate the frequency and coverage area of soil-based CDHEs using observational data, with only anthropogenically-driven changes in either soil moisture or temperature eliminated (Methods). The differences between these time series and the natural variability-induced evolutions of soil-based CDHEs represent the variations that can be only attributed to anthropogenic changes in soil temperature or moisture (Methods). Our results show that over the past four decades,

anthropogenic soil warming has increased the frequency and coverage area of soil-based CDHEs in China by 5.1 days and $195.3 \times 10^4 \text{ km}^2$, respectively (Fig. 4c, d). In contrast, anthropogenic changes in soil moisture have reduced soil-based CDHE frequency and coverage area by 0.6 days and $69.9 \times 10^4 \text{ km}^2$ (Fig. 4c, d). Notably, anthropogenic changes in soil temperature and moisture exhibit opposite trends in central-eastern and northern China (Supplementary Fig. 8c, d).

Consequently, the nonlinear interaction between these factors has further decreased soil-based CDHE frequency and coverage area by 2.5 days and $59.7 \times 10^4 \text{ km}^2$ (Fig. 4c, d). Collectively, these findings indicate that the observed increases in soil-based CDHE frequency and coverage area in China are predominantly driven by anthropogenic soil warming.

Growing impacts of soil-based CDHEs on vegetation productivity

To project the future risk of soil-based CDHEs in China, we use a single model initial-condition large ensemble (50 members) to minimize the influence of internal climate variability on simulated responses of these compound extremes to external forcings (Methods). Externally forced soil-based CDHEs in China exhibit a steadily increasing trend in frequency at a rate of approximately 0.6 days per decade from 1980 to 2017 (Fig. 5a–c), which is consistent with observational results (Fig. 2b). Under the Shared Socio-economic Pathway 1-2.6 (SSP1-2.6) emission scenario⁴², the regional mean frequency of externally forced soil-based CDHEs in China is projected to rise by the mid-twenty-first century, followed by a slight decline through the end of the twenty-first century (i.e., 2071–2100) (Fig. 5a). Under SSP2-4.5, the frequency of externally forced soil-based CDHEs will continue to increase until the 2080s, after which it will stabilize by the end of the twenty-first century (Fig. 5b). For the scenario characterized by uncurbed carbon emissions and heavy fossil fuel reliance (SSP5-8.5), soil-based CDHE frequency in China is projected to increase steadily and rapidly through the twenty-first century (Fig. 5c). Relative to the 1981–2010 baseline, the mean frequency of soil-based CDHEs in China is projected to increase by 4.1 (5–95% range: 2.6–5.8), 7.7 (5.6–10.4), and 13.3 (11.7–15.7) days by the end of the twenty-first century under SSP1-2.6, SSP2-4.5, and SSP5-8.5, respectively.

Spatially, a more substantial increase in externally forced soil-based CDHEs is projected for Central China under SSP1-2.6 (Supplementary Fig. 9a). Under SSP2-4.5 and SSP5-8.5, soil-based CDHE frequency is projected to increase markedly in Central and southern China (Supplementary Fig. 9b, c). Large swaths of northeastern and northwestern China may also experience a greater increase in soil-based CDHEs under SSP5-8.5. Given that most of China's croplands and forests are distributed in central, southern, and northeastern regions (Supplementary Fig. 10), croplands, forests, and shrubs are projected to face a substantially heightened risk of soil-based CDHEs (Fig. 5d–f). The projected frequency changes for barren lands and grasslands are roughly half of those for forests and shrubs. Besides, impervious surfaces are projected to exhibit considerable percentage changes in soil-based CDHE frequency under SSP1-2.6 and SSP2-4.5 (Fig. 5d, e).

These changes in soil-based CDHE frequency would amplify the impact of such extremes on vegetation productivity. Assuming the magnitude and spatial pattern of GPP responses to soil-based CDHEs (as shown in Fig. 1a) remain unchanged in the future, nationwide total GPP anomalies associated with soil-based CDHEs under SSP5-8.5 would deteriorate from $-0.009 \text{ Pg C a}^{-1}$ over 1981–2010 to $-0.025 \text{ Pg C a}^{-1}$ over 2071–2100 (Fig. 5g). This deterioration is notably more pronounced than that under low-to-median emission scenarios (SSP1-2.6 and SSP2-4.5; Fig. 5g). Under SSP1-2.6, with relatively moderate increases in soil-based CDHEs and a frequency trajectory that peaks and then declines (Fig. 5a), the magnitudes of end-of-century GPP anomalies related to soil-based CDHEs may be slightly lower than mid-century levels (Fig. 5g). These findings underscore that urgent efforts to achieve net-zero carbon emissions can deliver substantial ecological co-benefits.

Discussion

Our results reveal that the adverse effects of soil-based CDHEs on vegetation productivity in China are generally more pronounced than those of meteorological CDHEs. Over the past four decades, soil-based

CDHEs have become increasingly frequent at both local and regional scales in China, particularly in northern China. This surge is primarily driven by anthropogenic soil warming. Relative to the 1981–2010 baseline, soil-based CDHEs in China are projected to increase by 13.3 days by the end of the twenty-first century under a high-end emission scenario. Such an increase may reduce China's terrestrial vegetation GPP by approximately $0.025 \text{ Pg C a}^{-1}$. These findings suggest that the traditional assessments of the impacts of CDHEs on the terrestrial carbon sinks based on meteorological metrics may overlook and potentially underestimate the escalating ecological risks posed by soil-based CDHEs.

Soil-based CDHEs may also have broader implications, serving as a link between vegetation and soil ecosystems. Given these potential implications, more efforts are warranted to quantify the impacts of soil-based CDHEs on other environmental dimensions, including soil microbial and enzymatic activities⁴³, biodiversity⁴⁴, soil carbon sinks⁴⁵, and soil-borne pathogens⁴⁶. Furthermore, our findings lay a foundation for further understanding of the relationships between soil-based CDHEs, weather systems, and land-atmosphere interactions. This, in turn, could enhance the predictive skill of early warning systems⁴⁷ and help mitigate the damages and losses caused by soil-based CDHEs.

Our work underscores the importance of accounting for the soil-plant-atmosphere continuum when studying compound extremes in a changing climate. While we have revealed the impacts of soil-based CDHEs on vegetation productivity, the effects of terrestrial vegetation dynamics (e.g., greening) on soil-based CDHEs remain unclear and warrant further investigation. Additionally, surface soil temperature and moisture are closely interconnected with root-zone soil temperature and moisture via thermal and hydraulic conduction. Because surface soil moisture data are more constrained by station- and satellite-based observations than root-zone soil moisture data, our analysis focuses on surface-layer soil-based CDHEs. However, vegetation productivity may be more sensitive to changes in root-zone soil moisture and temperature, which requires further exploration.

We attribute the rapid increase in soil-based CDHEs predominantly to anthropogenically-driven large-scale soil warming. However, local factors, such as urbanization and other land cover changes, may also influence soil-based CDHEs by altering the land-surface energy budget and soil water content. For example, studies have shown that while anthropogenic large-scale warming primarily leads to the increased frequency and duration of CDHEs across U.S. cities, urban development exacerbates this effect⁴⁸. Further research is therefore needed to fully understand the drivers and impacts of soil-based CDHEs. Regarding model simulations, most soil moisture data derived from CMIP6 models (including MPI-GE-CMIP6) reasonably reproduce the spatiotemporal patterns of observations⁴⁹. Compared to cold zones, models provide more accurate estimates of soil moisture in temperate and tropical zones⁴⁹. Additionally, models better represent surface soil temperature than subsurface soil temperature. However, there is substantial inter-model spread in simulations of surface soil temperature in cold regions and during cold months (from January to April and from October to December)⁵⁰. This underscores the urgent need to explore how snow, ice, and freeze-thaw regulate the thermal states of the soils, as well as to collect more soil temperature observational data to improve model performance. Nevertheless, these limitations primarily affect soil temperature simulations during cold seasons, which have a relatively minor impact on warm-season soil-based CDHEs. For future projections, our assumption that vegetation does not undergo physiological acclimation to repeated soil-based CDHEs, along with the usages of static vegetation distributions and historical productivity responses, may overestimate future vegetation productivity sensitivity to soil-based CDHEs. On the other hand, as soil-based CDHEs generally become more intense in a warmer and drier future, the assumption of an invariant magnitude of GPP responses to soil-based CDHEs may result in an underestimation of

their impacts, as more intense events could trigger more severe physiological stress in vegetation than current observations suggest. Additionally, the omission of human interventions (e.g., agricultural activities, forest management, grazing) may introduce additional uncertainties into impact assessments, attribution analyses, and future projections. For instance, the GLEAM soil moisture dataset used in this study does not account for irrigation, which may lead to an underestimation of soil moisture levels in irrigated croplands. This could limit the accuracy of our results in intensively irrigated regions. Future work should integrate irrigation-related data and explicitly account for land-use practices to refine the assessments of soil moisture dynamics and vegetation responses to soil-based CDHEs.

Methods

Soil and climate datasets

We use a homogenized, gridded observational dataset of daily soil temperature⁵¹ covering the mainland of China from 1980 to 2017, with a horizontal resolution of 0.25°. This dataset was developed using raw daily soil temperature records from more than 2400 meteorological stations. Because the number of stations with valid data varies annually, a threshold-based missing-value criterion was applied to retain usable stations: (1) monthly data for a station are deemed missing if over nine days are missing in that month; (2) annual data are considered missing if there are more than three consecutive months of missing data. After excluding stations with more than 50% missing annual data, 2360 stations remained⁵¹. Raw soil temperature data contain non-climatic biases, which fall into two categories⁵¹. The first category comprises temporally concentrated biases induced by the transition from manual to automatic observation instruments at 197 stations in northern China in 2004. Because discrepancies between manual and automatic instruments are most pronounced under snowy conditions, these biases were most prominent during the cold season (October–April) in regions north of 40°N. To address this issue, regression equations relating surface soil temperature to high-quality surface air temperature were constructed for each month and each station during the pre-2004 period⁵¹. The derived regression coefficients were then used to reconstruct surface soil temperature data for the post-2004 period⁵¹. The relationship between surface soil temperature and surface air temperature can be modulated by other factors (e.g., precipitation frequency, solar radiation, vegetation). Consequently, using a single linear relationship between these two variables to correct the first category of non-climatic biases may introduce uncertainties. Nevertheless, these non-climatic biases primarily affect soil temperature data during cold months, which have only a minor impact on the identification of warm-season soil hot extremes. The second category consists of temporally scattered non-climatic biases arising from station relocations and changes in recording procedures. These were detected and fully corrected using the Multiple Analysis of Series for Homogenization method^{51,52}.

We employ daily soil moisture data derived from the latest version of the Global Land Evaporation Amsterdam Model (GLEAM4)⁵³, which covers the period 1980–2017 at a spatial resolution of 0.1°. This dataset was generated using algorithms that simulate key land surface and soil physical processes, forced by a combination of satellite-derived and reanalysis-based input data. Specifically, GLEAM4 utilizes a multi-layer running water balance model driven by precipitation observations⁵³. To correct for potential biases between modeled and observed soil moisture states, microwave-derived soil moisture observations in the topsoil layer are well assimilated. Our analysis focuses on surface-layer soil temperature and moisture, defined here as the top 10 cm of the soil profile.

Additionally, we use a high-resolution, gridded climate observation dataset (CN05.1)⁵⁴, which provides daily-scale relative humidity, surface air temperature, and precipitation at a spatial resolution of

0.25° for the mainland of China over the period 1980–2017. This dataset was developed using quality-controlled meteorological records from more than 2400 meteorological stations and a thin-plate smoothing spline interpolation technique. Based on the method in ref. 55, we calculate daily vapor pressure deficit (VPD) using the daily mean temperature and relative humidity data in CN05.1. Additionally, we use a global multi-timescale (5, 30, 90, and 180 days) daily Standardized Precipitation Evapotranspiration Index dataset⁵⁶, with a spatial resolution of 0.25° from 1982 to 2021. This dataset was developed based on the precipitation data from the fifth-generation ECMWF atmospheric reanalysis of the global climate and the potential evaporation from Singer's dataset. To facilitate computations, all datasets are remapped to a common 0.5° × 0.5° grid using local grid averaging, and grids containing missing values are masked out. Although local grid averaging is not a strictly conservative remapping technique, it is computationally efficient and yields gridded values of adequate accuracy.

Gross primary production, solar-induced chlorophyll fluorescence, and net primary production datasets

We use a gridded dataset of global daily estimates of gross primary production (GPP), with a spatial resolution of 0.05°. This dataset is hosted by the Oak Ridge National Laboratory Distributed Active Archive Center for Biogeochemical Dynamics⁵⁷. It was generated based on GPP observations from FLUXNET—a global network encompassing over 500 eddy covariance tower sites. Specifically, to upscale the FLUXNET-recorded GPP values to a global scale, neural networks were constructed using the Moderate Resolution Imaging Spectroradiometer (MODIS) MCD43C4v006 Nadir Bidirectional Reflectance Distribution Function (BRDF)-Adjusted Reflectance product.

Additionally, we use a satellite-retrieved global dataset of solar-induced chlorophyll fluorescence (SIF) under clear-sky conditions⁵⁸ to investigate the response of vegetation photosynthetic activity to soil temperature and moisture anomalies. This dataset was created by constructing a neural network, with inputs including surface reflectance from the MODIS and SIF observations from the Orbiting Carbon Observatory-2 (OCO-2). It has a spatial resolution of 0.05° and a temporal resolution of 4 days. To align with the temporal resolutions of soil datasets, the 4-day SIF time series is interpolated to a daily scale using a cubic spline interpolation algorithm. We choose to use GPP and SIF to analyze the impacts of soil-based CDHEs on vegetation productivity for two key reasons: first, both GPP and SIF datasets are observationally constrained, thereby ensuring relatively high accuracy; second, the consistent patterns of vegetation productivity responses to soil-based CDHEs derived from these two distinct datasets enhance the robustness of our findings.

We also utilize the land carbon flux dataset generated by the Más Informada Carnegie-Ames-Stanford-Approach (MiCASA) model⁵⁹, which provides global daily net primary production (NPP) data at a horizontal resolution of 0.1°. Within the MiCASA model, NPP is defined as the product of four core components: photosynthetically active solar radiation (PAR), the fractional absorption of PAR by the vegetation canopy (fPAR), a light utilization efficiency parameter, and variables representing moisture and temperature constraints. The model's input data include incident solar radiation, surface air temperature, precipitation, which were sourced from NASA Modern-Era Retrospective analysis for Research and Applications, Version 2, a soil type map, and several MODIS-based datasets, including land cover classification (MCD12Q1), burned area (MCD64A1), and Nadir BRDF-Adjusted Reflectance (MCD43A4).

The GPP, SIF, and NPP data are remapped to a common 0.5° × 0.5° grid using local grid averaging. We analyze the impacts of soil-based CDHEs on vegetation productivity over the period 2001–2017. This timeframe is the common overlapping period of the GPP, SIF, NPP, soil temperature and moisture datasets.

Geopotential, wind, and surface flux data

To identify the drivers of the non-uniform spatial pattern of frequency changes in soil-based CDHEs, we use monthly 500-hPa geopotential, zonal wind, and meridional wind data derived from the fifth-generation ECMWF atmospheric reanalysis of the global climate⁶⁰. To estimate the strength of soil moisture-temperature coupling, we use daily actual evaporation (E), potential evaporation (E_p), and sensible heat flux (H) data from the GLEAM4 dataset⁵³. All the data are remapped to a common $0.5^\circ \times 0.5^\circ$ grid using local grid averaging.

Land cover dataset

To project the area-weighted mean frequency changes of soil-based CDHEs for individual land cover types in China, we use a satellite-derived dataset of China's annual land cover distributions (CLCD)⁶¹ with a spatial resolution of 30 meters. The CLCD was generated by compiling training samples from pre-existing China's land-use/land-cover datasets and constructing a random forest classifier that incorporates 36 input features, including spectral bands, spectral indices, phenological metrics, topographic variables, and geographical location coordinates. Based on validation using over 5000 visually interpreted samples, the dataset achieves an overall accuracy of 79.3%, outperforming other pre-existing annual land cover datasets for China⁶¹. The CLCD classifies land surfaces into nine types: croplands, forests, shrubs, grasslands, water bodies, snow and ice, barren lands, impervious surfaces, and wetlands.

Model simulations

To quantify the contributions of anthropogenic changes in soil temperature and moisture to the observed increase in soil-based CDHEs, we use outputs from 9 CMIP6 climate models (Supplementary Table 1). These models provide monthly surface-layer soil moisture and total soil temperature from historical simulations driven by two forcing scenarios: ALL (incorporating both anthropogenic and natural forcings) and NAT (including only solar activities and volcanic aerosols)^{38,39}.

Since historical ALL-forced simulations end in 2014, we extend these simulations using future projections under SSP5-8.5 to cover the period 1980–2017. In contrast, NAT-forced simulations extend through 2020, requiring no additional extension. Within the CMIP6 framework, simulated surface-layer soil moisture is defined as water within the upper 10 cm of soil, consistent with soil moisture definition in the GLEAM4 dataset. Soil temperature, however, is modeled across multiple vertical layers, with layer boundaries and thicknesses varying across different CMIP6 models. To derive simulated surface 10-cm soil temperature (matching the vertical scope of observational soil temperature data), we interpolate the layered data to the 2.5-cm and 7.5-cm depths using vertical linear interpolation, and compute the arithmetic mean of these two depth-specific temperatures to represent the surface-layer soil temperature.

Additionally, we use initial-condition large-ensemble simulations from the Max Planck Institute Grand Ensemble with CMIP6 forcing (MPI-GE-CMIP6), produced by the MPI-ESM1.2-LR model⁶², to project future changes in the frequency of soil-based CDHEs in China. The MPI-GE-CMIP6 consists of 50 ensemble members, each initialized with slightly different initial conditions. Their evolutionary trajectories differ solely due to chaotic internal variability in the climate system. Given that the temporal sequence of internal variability in each ensemble member is randomly phased, the ensemble mean or median across all 50 members can effectively isolate and represent the externally forced changes. We select MPI-GE-CMIP6 because it is the only large-ensemble dataset in CMIP6 that provides daily-scale surface-layer soil moisture and total soil temperature data in historical ALL-forced simulations and future climate projections under SSP1-2.6, SSP2-4.5, and SSP5-8.5. All model outputs are regridded to the same standard $0.5^\circ \times 0.5^\circ$ grid adopted in previous analyses using linear interpolation.

Soil-based CDHE identification

A soil-based CDHE is identified when daily surface soil temperature exceeds its historical 90th percentile and daily surface soil moisture falls below its historical 10th percentile corresponding to the specific calendar day during warm seasons (from May to September). These historical percentiles are determined by sorting 15-day samples (including the target day itself, and 7 days prior to and subsequent to it) across the historical period (1981–2010), resulting in a total of 450 days (30 years \times 15 days). For a given calendar day d , the 90th and 10th percentile thresholds are computed from the data collections DC_{ST} and DC_{SM} , which are defined as:

$$DC_{ST} = U_{y=1981}^{2010} U_{i=d-7}^{d+7} ST_{i,y} \quad (1)$$

$$DC_{SM} = U_{y=1981}^{2010} U_{i=d-7}^{d+7} SM_{i,y} \quad (2)$$

where ST and SM denote soil temperature and moisture, respectively. i and y represent day and year, respectively.

Soil-based CDHEs can thus occur on any warm-season day. Our focus on warm season is motivated by the fact that vegetation exhibits higher productivity during this period, rendering it more susceptible to soil dryness and heat stress. Notably, the percentile-based event identification method also accounts for seasonal and intra-seasonal variability in the acclimation capability of vegetation to excessive soil dryness and heat. This is critical because vegetation's tolerance to such extremes may shift across the warm season (e.g., due to phenological stages like flowering or grain filling), and the 15-day window-based percentile calculation inherently captures these temporal shifts in vegetation's adaptive capacity.

Responses of GPP, SIF, and NPP to soil-based CDHEs

Elevated atmospheric CO_2 concentrations can stimulate photosynthesis (i.e., the CO_2 fertilization effect), driving long-term increasing trends in GPP, SIF, and NPP across many regions, including China. These CO_2 -driven trends may complicate or distort the assessment of vegetation responses to soil-based CDHEs. Thus, the impacts of CO_2 fertilization on vegetation productivity and photosynthetic activity must be removed prior to analysis. For each grid cell g and specific calendar day d , we perform linear regressions of daily raw GPP, SIF, and NPP time series individually against the monthly mean CO_2 concentrations provided by the Mauna Loa Observatory, Hawaii ($[CO_2]_m$)⁶³, for the month m that contains the target calendar day d . We then remove the signal associated with the long-term atmospheric CO_2 trend from the raw time series. Taking GPP as an example:

$$(b_{d,g}, a_{d,g}) = \text{reg}(GPP_{d,y,g}, [CO_2]_{m,y}) \quad (3)$$

$$\text{Signal}_{CO_2d,y,g} = b_{d,g} \times ([CO_2]_{m,y} - [CO_2]_{m,1}) \quad (4)$$

$$GPP'_{d,y,g} = GPP_{d,y,g} - \text{Signal}_{CO_2d,y,g} \quad (5)$$

where b and a represent the slope and intercept of the linear regression, respectively; "reg" denotes the linear regression function; y represents the year; Signal_{CO_2} refers to the signal associated with the long-term atmospheric CO_2 concentration trend; and GPP' represents GPP with the influence of long-term CO_2 concentration changes removed.

Then, we calculate the daily anomalies of GPP, SIF, and NPP by subtracting the climatological seasonal cycle from the daily series with CO_2 signal removed. For each valid grid cell, we compute the mean anomalies of GPP, NPP, and SIF for each percentile bin combination of soil temperature and moisture, and obtain the composite mean for all grid cells with valid values. In particular, to quantify the

potential impacts of soil-based CDHEs on vegetation productivity, we calculate grid-composite mean anomalies of GPP, SIF, and NPP for days when soil-based CDHEs occurred.

Soil moisture-temperature coupling

To determine the role of soil moisture-temperature coupling in shaping the spatial pattern of soil-based CDHE frequency changes, we calculate the daily coupling metric π_i proposed by ref. 12 as follows:

$$\pi_i = \frac{ST_i - \overline{ST}}{\sigma_{ST}} \times \left(\frac{H_i - \overline{H}}{\sigma_H} - \frac{H_{p,i} - \overline{H}_p}{\sigma_{H_p}} \right) \quad (6)$$

where ST_i , H_i and $H_{p,i}$ denote daily surface soil temperature, sensible heat flux, and potential sensible heat flux. \overline{ST} , \overline{H} , and \overline{H}_p represent their climatological means for the specific calendar day, and σ_{ST} , σ_H , and σ_{H_p} denote their corresponding standard deviations.

Potential sensible heat flux is not directly available in the GLEAM4 dataset, so we estimate it using E , E_p , and H :

$$H_p = H - \lambda(E_p - E) \quad (7)$$

where λ is the latent heat of vaporization (here taken as $2.5 \times 10^6 \text{ J kg}^{-1}$).

A positive π value indicates that a large portion of daily surface soil temperature variability can be related to the difference between actual sensible heat flux and potential sensible heat flux, which is primarily governed by surface soil moisture. In other words, a higher positive π value generally signifies stronger coupling between soil moisture and temperature.

Individual contributions of anthropogenic changes in soil temperature and moisture

Very few CMIP6 climate models provide daily-scale surface soil temperature and moisture data from historical simulations driven by ALL and NAT forcings. This data limitation hinders the direct attribution of anthropogenic forcings (including anthropogenic greenhouse gas emissions, aerosols, and large-scale land-use changes) to the observed frequency changes of soil-based CDHEs. To address this constraint, we develop an indirect attribution framework to quantify anthropogenic influences on soil-based CDHE frequency changes. Specifically, we first calculate grid-level multi-model ensemble mean differences in monthly soil temperature and moisture between historical ALL- and NAT-forced simulations ($\Delta ST_{m,y,g}$ and $\Delta SM_{m,y,g}$). Given the baseline differences between ALL- and NAT-forced simulations, we further compute anthropogenically-induced changes in soil temperature (soil moisture) as the differences between $\Delta ST_{m,y,g}$ ($\Delta SM_{m,y,g}$) and its respective value in the first year of the study period. These anthropogenically-induced changes are then subtracted from the observed daily soil temperature and moisture time series as follows:

$$ST'_{d,m,y,g} = ST_{d,m,y,g} - (\Delta ST_{m,y,g} - \Delta ST_{m,1,g}) \quad (8)$$

$$SM'_{d,m,y,g} = SM_{d,m,y,g} - (\Delta SM_{m,y,g} - \Delta SM_{m,1,g}) \quad (9)$$

where ST and SM denote surface soil temperature and moisture, and d , m , y , and g represent calendar day, month, year, and grid cell. Δ indicates the multi-model ensemble mean ALL-minus-NAT differences in soil temperature and moisture.

Based on this, we first estimate trends in the frequency and spatial coverage of soil-based CDHEs in China (b_o) using daily soil temperature and moisture data with anthropogenic signals removed ($ST'_{d,m,y,g}$ and $SM'_{d,m,y,g}$). A grid cell is defined as part of the affected area (coverage) if it experiences at least three soil-based CDHE days during a single warm season. These estimated changes are considered to be largely driven by natural climate variability. Next, we recalculate the

trends (b_{ST}) using unadjusted soil temperature data ($ST_{d,m,y,g}$) paired with adjusted soil moisture data ($SM'_{d,m,y,g}$). The difference between b_{ST} and b_o is thus regarded as the influence of anthropogenic soil temperature changes on trends in soil-based CDHE frequency and coverage area. Similarly, we estimate trends (b_{SM}) using adjusted soil temperature data ($ST'_{d,m,y,g}$) paired with unadjusted soil moisture data ($SM_{d,m,y,g}$). The difference between b_{SM} and b_o represents the effects of anthropogenic soil moisture changes on the observed trends. Finally, we calculate the trends in frequency and coverage area (b) using the unadjusted, original daily soil temperature and moisture observation data. Trends induced by nonlinear interactions between anthropogenic soil temperature and moisture changes (b_{nl}) are estimated as:

$$b_{nl} = b - b_{ST} - b_{SM} + b_o \quad (10)$$

Projection of soil-based CDHE frequency changes

We use large-ensemble simulations and projections from the MPI-GE-CMIP6 to estimate future changes in the frequency of soil-based CDHEs in China. Soil-based CDHEs are identified for each day, grid cell, and ensemble member using the same methodology as adopted in the observational analysis. We calculate the area-weighted mean frequency of soil-based CDHEs, and estimate the frequency changes relative to the 1981–2010 baseline for each ensemble member and each emission scenario (SSP1-2.6, SSP2-4.5, and SSP5-8.5). This allows us to derive the ensemble median frequency changes of soil-based CDHEs under different emission scenarios.

We further project area-weighted mean changes in soil-based CDHE frequency for each major land cover type. Using the 2018 CLCD data, we first calculate the areal fraction of each of the nine major land covers within each grid cell ($LCF_{g,k}$), defined as the number of pixels belonging to a specific land cover divided by the total number of pixels in that grid cell. Note that 2018 CLCD data is used to approximate future land cover spatial distribution, which may differ from current conditions. We then estimate the regional mean frequency of soil-based CDHEs for each land cover type ($F_{k,y}$) as:

$$F_{k,y} = \frac{\sum_{g=1}^n LCF_{g,k} \times Area_g \times F_{g,y}}{\sum_{g=1}^n LCF_{g,k} \times Area_g} \quad (11)$$

where $Area$ denotes the geographic area of grid cell g . k and y represent land cover type and calendar year, respectively. $F_{g,y}$ is the soil-based CDHE frequency for grid cell g in year y .

Given that water bodies have no surface soils (thus no soil-based CDHEs), warm-season CDHEs barely affect snow and ice, and wetlands occupy a small total area in China, we focus our land cover-specific projections on six major types: croplands, forests, shrubs, grasslands, barren lands, and impervious surfaces. For these types, we estimate soil-based CDHE frequency changes (relative to the 1981–2010 baseline) by the end of the twenty-first century (2071–2100) under each emission scenario.

To link future soil-based CDHEs to vegetation productivity impacts, we first derive future soil-based CDHE frequency for each grid cell, year, ensemble member, and emission scenario ($f_{g,y,mem,sce}$) by adding the projected frequency changes to the observed climatological mean CDHE frequency over 1981–2010. Assuming that the magnitude and spatial pattern of GPP response to soil-based CDHEs remain unchanged in the future (a common simplification in impact projections when future acclimation mechanisms are not explicitly modeled), we calculate total GPP anomalies associated with soil-based CDHEs as the product of future soil-based CDHE frequency and the

composite mean GPP anomaly during the days with soil-based CDHEs:

$$\text{GPPfano}_{g,y,\text{mem},\text{sce}} = f_{g,y,\text{mem},\text{sce}} \times \text{GPPano}_{\text{comp}} \quad (12)$$

where *GPPfano* denotes future GPP anomalies, and *g*, *y*, *mem*, and *sce* represent the specific grid cell, year, ensemble member, and emission scenario, respectively. *f* indicates the frequency of soil-based CDHEs, and *GPPano_{comp}* denotes the composite mean GPP anomaly during soil-based CDHEs (Fig. 1a).

Statistical methods

We use the non-parametric Theil–Sen trend estimation method⁶⁴ to calculate linear trends. This method is robust to outliers and non-normal distributions. The non-parametric two-sided Mann–Kendall trend test^{65,66} is applied to assess the statistical significance of all derived trends. The 95% confidence intervals of the trends are estimated based on the Theil test⁶⁷.

Reporting summary

Further information on research design is available in the Nature Portfolio Reporting Summary linked to this article.

Data availability

All data supporting the findings are publicly available. The gridded daily soil temperature data are available at <https://www.scidb.cn/en/detail?dataSetId=765528002485288960&version=V3>. The GLEAM4 dataset (soil moisture, surface sensible and latent heat fluxes) is from <https://www.gleam.eu/>. The GPP, SIF, and NPP data can be downloaded from https://daac.ornl.gov/VEGETATION/guides/FluxSat_GPP_FPAR.html, <https://doi.org/10.6084/m9.figshare.6387494>, and https://acdsc.gsfc.nasa.gov/data/CMS/MICASA_FLUX_D.1, respectively. The CN05.1 data can be secured through <https://ccrc.iap.ac.cn/resource/detail?id=228>. The global daily SPEI dataset is available at <https://doi.org/10.5281/zenodo.8060268>. The ERA5 reanalysis data is available at <https://www.ecmwf.int/en/forecasts/dataset/ecmwf-reanalysis-v5>. The land-use/land-cover dataset is available at <https://zenodo.org/records/4417810>. The model simulation data can be downloaded from <https://pcmdi.llnl.gov/CMIP6/>. The raw data to reproduce the figures of the paper are available at <https://doi.org/10.6084/m9.figshare.28415420>⁶⁸.

Code availability

The codes supporting this study are available at <https://doi.org/10.6084/m9.figshare.28415420>⁶⁸.

References

- Hao, Y. et al. Probabilistic assessments of the impacts of compound dry and hot events on global vegetation during growing seasons. *Environ. Res. Lett.* **16**, 074055 (2021).
- Zhao, H. et al. U.S. winter wheat yield loss attributed to compound hot-dry-windy events. *Nat. Commun.* **13**, 7233 (2022).
- Richardson, D. et al. Global increase in wildfire potential from compound fire weather and drought. *npj Clim. Atmos. Sci.* **5**, 23 (2022).
- Yin, J. et al. Future socio-ecosystem productivity threatened by compound drought–heatwave events. *Nat. Sustain.* **6**, 259–272 (2023).
- Yao, Y. et al. Compound hot-dry events greatly prolong the recovery time of dryland ecosystems. *Natl. Sci. Rev.* **11**, nwa274 (2024).
- Jiang, L. et al. Increased frequency and severity of global compound dry and heat wave events in a daily scale. *J. Hydrol.* **654**, 132857 (2025).
- Chen, D. et al. Contribution of anthropogenic influence to the 2022-like Yangtze River valley compound heatwave and drought event. *npj Clim. Atmos. Sci.* **7**, 172 (2024).
- Tripathy, K. P. & Mishra, A. K. How unusual is the 2022 European Compound Drought and Heatwave Event? *Geophys. Res. Lett.* **50**, e2023GL105453 (2023).
- Tripathy, K. P., Mukherjee, S., Mishra, A. K., Mann, M. E. & Williams, A. P. Climate change will accelerate the high-end risk of compound drought and heatwave events. *Proc. Natl. Acad. Sci. USA* **120**, e2219825120 (2023).
- Hao, Z. et al. Compound droughts and hot extremes: characteristics, drivers, changes, and impacts. *Earth Sci. Rev.* **235**, 104241 (2022).
- Seneviratne, S. I. et al. Investigating soil moisture-climate interactions in a changing climate: a review. *Earth Sci. Rev.* **99**, 125–161 (2010).
- Miralles, D. G., van den Berg, M. J., Teuling, A. J. & de Jeu, R. A. M. Soil moisture-temperature coupling: a multiscale observational analysis. *Geophys. Res. Lett.* **39**, L21707 (2012).
- Alizadeh, M. R. et al. A century of observations reveals increasing likelihood of continental-scale compound dry-hot extremes. *Sci. Adv.* **6**, eaaz4571 (2020).
- Zscheischler, J. & Seneviratne, S. I. Dependence of drivers affects risks associated with compound events. *Sci. Adv.* **3**, e1700263 (2017).
- Zeng, J. et al. Comparison of the risks and drivers of compound hot-dry and hot-wet extremes in a warming world. *Environ. Res. Lett.* **19**, 114026 (2024).
- Zhang, X. et al. Amplification of coupled hot-dry extremes over eastern monsoon China. *Earth's Future* **11**, e2023EF003604 (2023).
- Fan, Y. et al. A critical review for real-time continuous soil monitoring: advantages, challenges, and perspectives. *Environ. Sci. Technol.* **56**, 13546–13564 (2022).
- Pastorello, G. et al. The FLUXNET2015 dataset and the ONEFlux processing pipeline for eddy covariance data. *Sci. Data* **7**, 225 (2020).
- Jiang, M. et al. Seamless global daily soil moisture mapping using deep learning based spatiotemporal fusion. *Int. J. Appl. Earth Obs.* **139**, 104517 (2025).
- Pokhrel, Y. et al. Global terrestrial water storage and drought severity under climate change. *Nat. Clim. Change* **11**, 226–233 (2021).
- Hosseinzadehtalaei, P., Termonia, P. & Tabari, H. Projected changes in compound hot-dry events depend on the dry indicator considered. *Commun. Earth Environ.* **5**, 220 (2024).
- García-García, A. et al. Soil heat extremes can outpace air temperature extremes. *Nat. Clim. Change* **13**, 1237–1241 (2023).
- Liu, L. et al. Soil moisture dominates dryness stress on ecosystem production globally. *Nat. Commun.* **11**, 4892 (2020).
- Li, W. et al. Widespread increasing vegetation sensitivity to soil moisture. *Nat. Commun.* **13**, 3959 (2022).
- Sharma, P. K. & Kumar, S. Soil temperature and plant growth. *Springer, Cham*. 175–204 (2023).
- Liu, Y. et al. Soil temperature dominates forest spring phenology in China. *Agric. Meteorol.* **355**, 110141 (2024).
- Wang, C. et al. The temperature sensitivity of soil: microbial biodiversity, growth, and carbon mineralization. *ISME J.* **15**, 2738–2747 (2021).
- Hursh, A. et al. The sensitivity of soil respiration to soil temperature, moisture, and carbon supply at the global scale. *Glob. Change Biol.* **23**, 2090–2103 (2017).
- Yuan, D. et al. Species-specific indication of 13 tree species growth on climate warming in temperate forest community of northeast China. *Ecol. Indic.* **133**, 108389 (2021).
- Ridder, N. N. et al. Global hotspots for the occurrence of compound events. *Nat. Commun.* **11**, 5956 (2020).
- Vicente-Serrano, S. M., Beguería, S. & López-Moreno, J. I. A. Multi-scalar drought index sensitive to global warming: the Standardized

- Precipitation Evapotranspiration Index. *J. Clim.* **23**, 1696–1718 (2010).
32. Törnros, T. & Menzel, L. Addressing drought conditions under current and future climates in the Jordan River region. *Hydrol. Earth Syst. Sci.* **18**, 305–318 (2014).
 33. Wang, H., Rogers, J. C. & Munroe, D. K. Commonly used drought indices as indicators of soil moisture in China. *J. Hydrometeor.* **16**, 1397–1408 (2015).
 34. Gevaert, A. I., Miralles, D. G., de Jeu, R. A. M., Schellekens, J. & Dolman, A. J. Soil moisture-temperature coupling in a set of land surface models. *J. Geophys. Res. Atmos.* **123**, 1481–1498 (2018).
 35. Yuan, Q. et al. Coupling of soil moisture and air temperature from multiyear data during 1980–2013 over China. *Atmosphere* **11**, 25 (2020).
 36. Abu-Hamdeh, N. H. Thermal properties of soils as affected by density and water content. *Biosyst. Eng.* **86**, 97–102 (2003).
 37. Al-Kayssi, A. W., Al-Karaghoul, A. A., Hasson, A. M. & Beker, S. A. Influence of soil moisture content on soil temperature and heat storage under greenhouse conditions. *J. Agric. Eng. Res.* **45**, 241–252 (1990).
 38. Gillett, N. P. et al. The Detection and Attribution Model Intercomparison Project (DAMIP v1.0) contribution to CMIP6. *Geosci. Model Dev.* **9**, 3685–3697 (2016).
 39. Eyring, V. et al. Overview of the Coupled Model Intercomparison Project phase 6 (CMIP6) experimental design and organization. *Geosci. Model Dev.* **9**, 1937–1958 (2016).
 40. Bevacqua, E. et al. Precipitation trends determine future occurrences of compound hot-dry events. *Nat. Clim. Chang.* **12**, 350–355 (2022).
 41. Hong, H., Sun, J. & Wang, H. Interdecadal variation in the frequency of extreme hot events in Northeast China and the possible mechanism. *Atmos. Res.* **244**, 105065 (2020).
 42. Meinshausen, M. et al. The shared socio-economic pathway (SSP) greenhouse gas concentrations and their extensions to 2500. *Geosci. Model Dev.* **13**, 3571–3605 (2020).
 43. Jansson, J. K. & Hofmockel, K. S. Soil microbiomes and climate change. *Nat. Rev. Microbiol.* **18**, 35–46 (2020).
 44. Robinson, S. I., McLaughlin, ÓB., Marteinsdóttir, B. & O’Gorman, E. J. Soil temperature effects on the structure and diversity of plant and invertebrate communities in a natural warming experiment. *J. Anim. Ecol.* **87**, 634–646 (2018).
 45. Bossio, D. A. et al. The role of soil carbon in natural climate solutions. *Nat. Sustain.* **3**, 391–398 (2020).
 46. Delgado-Baquerizo, M. et al. The proportion of soil-borne pathogens increases with warming at the global scale. *Nat. Clim. Chang.* **10**, 550–554 (2020).
 47. Neußner, O. Early warning alerts for extreme natural hazard events: a review of worldwide practices. *Int. J. Disaster Risk Reduct.* **60**, 102295 (2021).
 48. Ghanbari, M. et al. The role of climate change and urban development on compound dry-hot extremes across US cities. *Nat. Commun.* **14**, 3509 (2023).
 49. Liu, Y., Chen, X., Bai, Y. & Zeng, J. Evaluation of 22 CMIP6 model-derived global soil moisture products of different shared socio-economic pathways. *J. Hydrol.* **636**, 131241 (2024).
 50. Zhou, J., Zhang, J. & Huang, Y. Evaluation of soil temperature in CMIP6 multimodel simulations. *Agric. Meteorol.* **352**, 110039 (2024).
 51. Wang, D., Wang, A. & Kong, X. Homogenization of the daily land surface temperature over the mainland of China from 1960 through 2017. *Adv. Atmos. Sci.* **38**, 1811–1822 (2021).
 52. Szentimrey, T. Overview of mathematical background of homogenization, summary of method MASH and comments on benchmark validation. *Int. J. Climatol.* **43**, 6314–6329 (2023).
 53. Miralles, D. G. et al. GLEAM4: global land evaporation and soil moisture dataset at 0.1° resolution from 1980 to near present. *Sci. Data* **12**, 416 (2025).
 54. Wu, J. & Gao, X. A gridded daily observation dataset over China region and comparison with the other datasets. *Chin. J. Geophys.* **56**, 1102–1111 (2013).
 55. Yuan, W. et al. Increased atmospheric vapor pressure deficit reduces global vegetation growth. *Sci. Adv.* **5**, eaax1396 (2019).
 56. Liu, X. et al. The first global multi-timescale daily SPEI dataset from 1982 to 2021. *Sci. Data* **11**, 223 (2024).
 57. Joiner, J. et al. Estimation of terrestrial global Gross Primary Production (GPP) with satellite data-driven models and eddy covariance flux data. *Remote Sens.* **10**, 1346 (2018).
 58. Zhang, Y., Joiner, J., Alemohammad, S. H., Zhou, S. & Gentine, P. A global spatially contiguous solar-induced fluorescence (CSIF) dataset using neural networks. *Biogeosciences* **15**, 5779–5800 (2018).
 59. Randerson, J. T., Thompson, M. V., Malmstrom, C. M., Field, C. B. & Fung, I. Y. Substrate limitations for heterotrophs: implications for models that estimate the seasonal cycle of atmospheric CO₂. *Glob. Biogeochem. Cycles* **10**, 585–602 (1996).
 60. Hersbach, H. et al. The ERA5 global reanalysis. *Q. J. Roy. Meteorol. Soc.* **146**, 1999–2049 (2020).
 61. Yang, J. & Huang, X. The 30 m annual land cover dataset and its dynamics in China from 1990 to 2019. *Earth Syst. Sci. Data* **13**, 3907–3925 (2021).
 62. Olonscheck, D. et al. The new Max Planck Institute Grand Ensemble with CMIP6 forcing and high-frequency model output. *J. Adv. Model Earth. Syst.* **15**, e2023MS003790 (2023).
 63. Keeling, C. D. et al. Atmospheric carbon dioxide variations at Mauna Loa Observatory, Hawaii. *Tellus* **28**, 538–551 (1976).
 64. Sen, P. K. Estimates of the regression coefficient based on Kendall’s tau. *J. Am. Stat. Assoc.* **63**, 1379–1389 (1968).
 65. Mann, H. B. Nonparametric tests against trend. *Econometrica* **13**, 245–259 (1945).
 66. Kendall, M. G. *Rank Correlation Methods* (Griffin, 1975).
 67. Hollander, M. & Wolfe, D. *Nonparametric Statistical Methods* Ch 9, 207–208 (John Wiley & Sons, 1973).
 68. Liang, et al. Anthropogenically-driven escalating impact of soil-based compound dry-hot extremes on vegetation productivity. figshare. Dataset. <https://doi.org/10.6084/m9.figshare.28415420> (2025).

Acknowledgements

Our sincere gratitude goes to the researchers and institutions responsible for the development, compilation, and public release of the datasets employed in this study. Their efforts in advancing open data sharing have laid a critical foundation for this work. This work was supported by the National Natural Science Foundation of China (42522102, 42275040) and the Programme of Kezhen-Bingwei Excellent Young Scientists of the Institute of Geographic Sciences and Natural Resources Research, Chinese Academy of Sciences (2022RC006).

Author contributions

J.W. and Q.G. conceived and designed the study. Y.L. and J.W. performed the analyses. J.W. and Y.L. wrote the draft. J.W., Q.G., Z.H., H.W., and H.C. reviewed, revised, and edited the manuscript. All authors contributed to interpreting the results.

Competing interests

The authors declare no competing interests.

Additional information

Supplementary information The online version contains supplementary material available at <https://doi.org/10.1038/s41467-026-68878-3>.

Correspondence and requests for materials should be addressed to Jun Wang or Quansheng Ge.

Peer review information *Nature Communications* thanks Wanjuan Song, Duminda Vidana and the other anonymous, reviewer(s) for their contribution to the peer review of this work. A peer review file is available.

Reprints and permissions information is available at <http://www.nature.com/reprints>

Publisher's note Springer Nature remains neutral with regard to jurisdictional claims in published maps and institutional affiliations.

Open Access This article is licensed under a Creative Commons Attribution-NonCommercial-NoDerivatives 4.0 International License, which permits any non-commercial use, sharing, distribution and reproduction in any medium or format, as long as you give appropriate credit to the original author(s) and the source, provide a link to the Creative Commons licence, and indicate if you modified the licensed material. You do not have permission under this licence to share adapted material derived from this article or parts of it. The images or other third party material in this article are included in the article's Creative Commons licence, unless indicated otherwise in a credit line to the material. If material is not included in the article's Creative Commons licence and your intended use is not permitted by statutory regulation or exceeds the permitted use, you will need to obtain permission directly from the copyright holder. To view a copy of this licence, visit <http://creativecommons.org/licenses/by-nc-nd/4.0/>.

© The Author(s) 2026